

Modeling of the Internal Two-Phase Flow in a Gas-Centered Swirl Coaxial Fuel Injector

Nathaniel Trask^{*}, J. Blair Perot^{*}, David P. Schmidt^{*},
Terry Meyer[†], Malissa Lightfoot[‡], Steven Danczyk[‡]

Predicting the liquid film dynamics inside the injector cup of gas-centered swirl coaxial fuel injectors requires a general two-phase approach that is appropriate for all liquid volume fractions, high Weber number, and complex geometries. The rapid exchange of momentum at the highly convoluted interface requires tight numerical coupling between the gas and liquid phases. An Eulerian two-phase model is implemented to represent the liquid and gas interactions in the injector as well as the atomization processes at the rough interface. The model, originally proposed by Vallet et al, assumes that in the limit of infinite Reynolds and Weber number, features of the atomization process acting at large length scales are separable from small scale mechanisms. A transport equation for the liquid volume fraction represents the dispersion of the liquid into the gas via a traditional turbulent diffusion hypothesis. A model for the growth of mean interfacial surface area is then used to characterize the growth of instability at the interface, allowing a characterization of Sauter mean diameter. The model shows promise as a computationally inexpensive tool for characterizing spray quality in regions where optical experimental data are difficult to obtain and two-phase direct numerical simulation methods are too demanding. Two-dimensional results of the model are compared to photographs of the liquid film within the injector cup. The comparisons show good agreement between the predicted film profile and experimental measurements, although in some cases underpredicting the film length. The discrepancy between the experiment and model results suggest the need to extend the inter-phase coupling to a form more suitable for anisotropic, swirling flow.

Introduction

Fuel injection elements in modern rocket propulsion systems operate at extremely high Reynolds and Weber number, producing a wide range of relevant length scales. Rendering these disparate length scales with direct numerical simulation techniques is extremely expensive, since the mesh resolution would need to be fine enough to resolve the smallest droplets yet have an extent that spans the entire nozzle. Experimental techniques, though able to provide macroscopic insights, have difficulty quantifying the small scale features of the spray formation due to the primary atomization zones topological complexity and optically dense nature.

Gas-centered swirl-coaxial injectors (GCSC) are particularly challenging to characterize due to the fact that atomization occurs within a small, visually obscured cup and is accompanied by a fully three-dimensional flow. The injector functions by injecting high velocity gaseous oxidizer axially through the center of the element, while liquid propellant is injected tangentially along the element wall to produce a swirling liquid film. A spray is formed by a combination of instability growth along the surface of the film and shear induced by the high velocity co-flowing gas. Although the injector resembles other injection schemes such as pressure-swirl and coaxial injectors, the GCSC differs in that the atomization occurs within the injector cup before the liquid enters the combustion chamber, without forming a conical sheet under typical operating conditions. To effectively predict atomization quality, it is essential both to predict the uniformity of the spray and to accurately predict film length. For designs in which the injector cup is significantly longer

^{*}University of Massachusetts at Amherst

[†]Iowa State University

[‡]Air Force Research Lab, Edwards Air Force Base

than the film length, overheating of the injector faceplate can occur. For cup lengths shorter than the film, incomplete atomization may occur.¹

In an extension of their 2006 paper in which they outline general mechanisms by which atomization takes place, Lightfoot et al. published a report in which they determine the relevant processes at play within the GCSC. They suggest, based on an inviscid linear instability analysis,² that liquid instability growth cannot be a dominant mechanism based on the prediction that few waves would reach a height capable of causing atomization, and that they would only be capable of atomizing approximately 2.5% of the total film volume. Under similar arguments, they also suggest that liquid-phase turbulence cannot be a dominating factor, and that the dominant mechanism taking place is the impact of gas-phase turbulent structures with the liquid interface.

Based on this assumption, they propose a model by which cylindrical gas eddies “scoop” out a disturbance in the liquid. Although the majority of the assumptions made are only to give a rough characterization of entrainment rate, they propose a useful criterion for gas turbulence driven atomization to occur: the kinetic energy of the turbulent eddy must exceed the surface tension energy of the interface.

$$\rho_g v_{eddy}^2 \geq \frac{\sigma}{d_{eddy}} \quad (1)$$

They use this equation to develop a criteria to judge what fraction of eddies are large enough to cause stripping, and use turbulence data from fully developed pipe flow to estimate an eddy size distribution. This relation is also useful for verifying the assumption that gas-phase turbulence is dominant. Under the assumption that the dominant eddies lie within the range of the larger, energy containing scale, the characteristic length and velocity scales are³

$$L = \frac{k^{\frac{3}{2}}}{\epsilon} \quad (2)$$

$$U = k^{\frac{1}{2}} \quad (3)$$

The assumption that d_{eddy} and v_{eddy} are on the order of L and U respectively, gives the following relation

$$\frac{k_g^{\frac{5}{2}}}{\epsilon_g} \geq C \frac{\sigma}{\rho_g} \quad (4)$$

Lightfoot et al. later performed experiments upon a variety of GCSC geometries to obtain measurements of film length as a function of relevant non-dimensional groups, such as momentum flux ratio and mixture ratio. Figure 1 demonstrates the range of geometry considered and a sample correlation.

Lightfoot’s work provides a quantitative characterization of the film within the injector cup. Downstream measurements of atomization quality have been performed over a wide variety of operating conditions over the past decade. For example, Rahman et al. performed hot and cold experiments of a GCSC to obtain visualizations of the spray structure and measurements of the pressure drop across the element,⁴ obtaining spray angle measurements but no direct calculations of droplet size. In a preliminary assessment of the potential of the GCSC versus traditional coaxial injectors Cohn et al. used a laser based Doppler interferometer to obtain measurements of droplet size and velocity, obtaining a range of diameters from $3.8 \mu m$ to $440 \mu m$ during typical operating conditions.⁵ Soltani et al. investigated sprays produced by a liquid-liquid GCSC in a non-combusting environment to obtain measurements of average droplet size and velocity, noting that both quantities achieve a self-similar structure.⁶

The effort described below focuses on the internal flow of a GCSC injector, and attempts to predict its ability to perform over a wide range of operating conditions, characterizing the internal flow. In the current work, simulations will be used to estimate the liquid film length and shape, particularly to predict whether the film reaches the end of the cup. Lightfoot et al.’s past investigations have shown these film characteristics to be very strongly correlated with the performance of the injector.¹ In the current work, a closely-coupled two-phase Eulerian method is investigated and used to predict the models applicability to GCSC operating conditions.

Experimental Study

Experimental data was collected using an injector body composed of acrylic. This acrylic body is modular, allowing differing injector geometries to be tested. Nominally, the outlet diameter of the injector is 19.05 mm

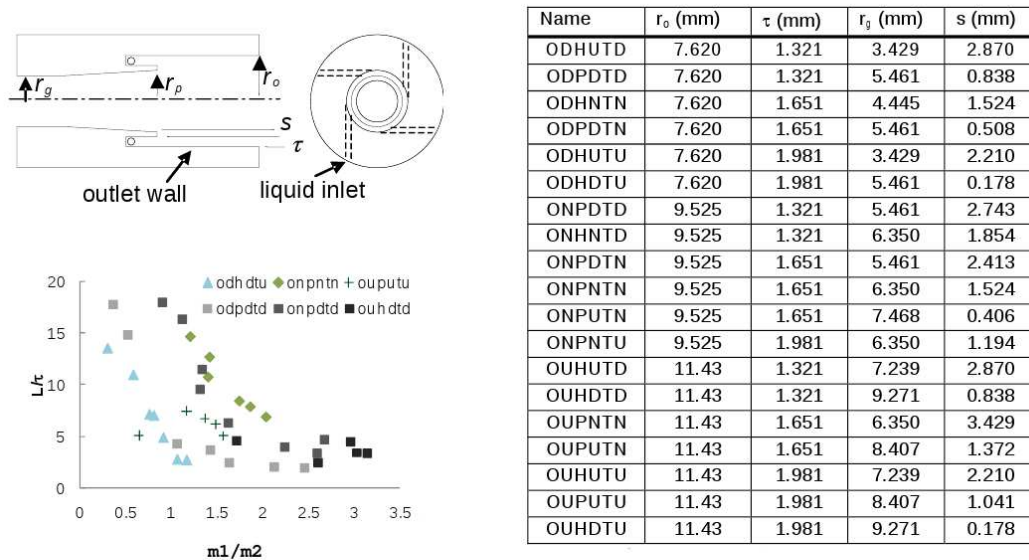


Figure 1. Top left: GCSC geometric parameters. Top Right: Dimensions of tested inserts. Bottom Left: Film length over initial film height as a function of mixture ratio.¹

(0.75 inches). The initial film thickness is nominally 1.65 mm (0.065 inches) with the step separating the gas and liquid having a height of 1.52 mm (0.06 inches). Upstream of the modular acrylic section is a stainless steel section which consists of 180 mm of gas inlet with a fixed radius of 6.35 mm (0.25 inches). All tests were performed with atmospheric back pressure using working fluids (simulants) of water and nitrogen at room temperature. The gas flow rates were varied from 0.0187-0.0798 kg/s. The liquid flow rates were varied from 0.0236-0.0794 kg/s. The momentum flux ratio, defined using the mass flow rates along with flow areas based on the initial film thickness for the liquid and the average gas post height $-(r_p + r_o)/2 = r_p + (s + \tau)/2$ – varied from around 10 to around 1100. Film length was determined from video images. For lighting, a laser beam was split and expanded into two sheets which were oriented 180° from one another along the centerline of the injector or spray. A Vision Research Phantom v7.3 camera positioned 90° from the laser sheets captured the images at 6006 fps with an exposure time of 150 microseconds. A typical image, with flow from left to right, is shown in Fig. 2. An in-house Matlab code was used to determine the film profile in each image using the change in intensity to determine the film boundary. Once the film profile has been determined, the code uses input information about the wall location to determine film length. Because the film length is not steady, the profiles extracted from 5000 images are averaged together to determine an average film length (and standard deviation). Analysis shows that 5000 images are sufficient to give good statistical results. Sample profiles are shown in Fig. 3.

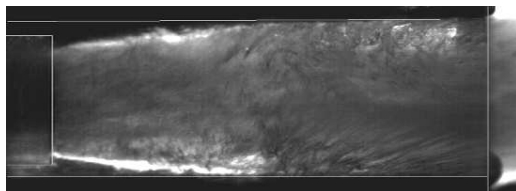


Figure 2. A typical image from the in-cup video is shown here. The edges of the injector body are highlighted including the sheltering lip.

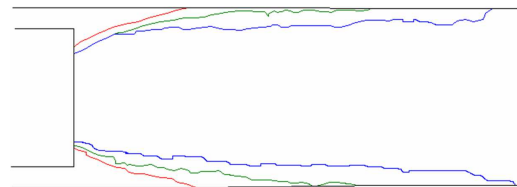


Figure 3. Representative profiles of a long, medium and short film. These profiles are from the geometry shown in Fig. 2 at momentum flux ratios of 110, 484 and 823 respectively

Modeling Approach

The modeling approach used in the current work recognizes that typical injector flows operate at extremely high Reynolds and Weber numbers. The so-called $\Sigma - Y$ model, originally proposed by Vallet et al.,⁷ assumes a separation of the large and small scales, allowing the bulk fluid motion to be directly simulated while the sub-grid features of the flow are resolved via modeling closures similar to those used in RANS turbulence modeling. Unlike Volume of Fluid (VOF), the $\Sigma - Y$ model does not attempt to reconstruct the highly convoluted interface. A VOF approach would be appropriate if one were intent on direct numerical simulation and willing to apply a micron-level mesh to any part of the domain where small droplets might exist. Taking advantage of this scale separation allows complex flows to be characterized with significantly less computational resources.

The original model proposed by Vallet is founded on four assumptions:

- Surface tension and viscosity act only at small length scales, which corresponds to infinite Reynolds and Weber numbers. This implies that the large scale features of the flow will be dependent only upon density variations. The surface tension and viscosity will only have an effect upon the small scale features.
- Although the small scale velocity fluctuations of the flow are unpredictable at the desired resolutions, the mean velocity field can be predicted using standard turbulence closures, such as the classical two equation k-epsilon model.
- The dispersion of the liquid phase into the gaseous phase can be modeled via a turbulent diffusion flux.
- The mean geometry of the liquid structures can be characterized by tracking the mean surface area of the liquid-gas interface per unit volume

To track the dispersion of the liquid phase an indicator function Y is introduced with value 1 in the liquid phase and 0 in the gas phase. The mean liquid volume fraction of the fluid is then given as \bar{Y} , and the mean mass averaged fraction is defined as $\tilde{Y} = \frac{\bar{\rho} \bar{Y}}{\rho}$. The transport equation for \tilde{Y} then takes the form:

$$\frac{\partial \tilde{\rho} \tilde{Y}}{\partial t} + \frac{\partial \tilde{\rho} \tilde{u}_i \tilde{Y}}{\partial x_j} = - \frac{\partial \tilde{\rho} \tilde{u}_i' \tilde{Y}'}{\partial x_i} \quad (5)$$

where u' denotes the turbulent fluctuations in velocity and Y' denotes turbulent fluctuations in volume fraction.

The value of \tilde{Y} is related to ρ by

$$\frac{1}{\rho} = \frac{\tilde{Y}}{\rho_{liq}} + \frac{1 - \tilde{Y}}{\rho_{gas}} \quad (6)$$

Treating the transport equation in this way allows the momentum equation to be solved using the single equation:

$$\frac{\partial \tilde{\rho} \tilde{u}_j}{\partial t} + \frac{\partial \tilde{\rho} \tilde{u}_i \tilde{u}_j}{\partial x_i} = - \frac{\partial \tilde{p}}{\partial x_j} - \frac{\partial \tilde{\rho} \tilde{u}_i' \tilde{u}_j'}{\partial x_i} \quad (7)$$

The turbulent diffusion liquid flux $\tilde{u}_i' \tilde{Y}'$ captures the effect of the relative velocity between the two phases. Models for both the turbulent diffusion liquid flux in the transport equation and the turbulent diffusion flux in the momentum equation must be formed to obtain closure. The further assumption that both the gas and liquid density is constant closes the system. Most previous implementations of the ΣY model use a classical compressible $k - \epsilon$ model to close the turbulent diffusion term, although Demoulin et al. proposed a modification of the transport equation to capture the effects of a large density gradient on the production of kinetic energy.⁸

With the large scale flow features described, a transport equation for the evolution of the interfacial surface area determines the small scale behavior of the flow. There have been several different forms suggested for this equation. A rigorous derivation of the equation from first principles has been performed by Morel.⁹ The transport equation of $\tilde{\Sigma}$ proposed by Vallet¹⁰ takes the same form as Morel's generalized derivation, having terms capturing the effects of convection, diffusion, surface stretching and coalescence.

$$\frac{\partial \bar{\Sigma}}{\partial t} + \frac{\partial u_j \bar{\Sigma}}{\partial x_j} = \frac{\partial}{\partial x_j} \left(D_{\Sigma} \frac{\partial \bar{\Sigma}}{\partial x_j} \right) + \frac{1}{\tau_{prod}} \bar{\Sigma} - \frac{1}{\tau_{destr}} \bar{\Sigma}^2 \quad (8)$$

τ_{prod} is a time scale representing the rate at which turbulence creates surface area, and τ_{destr} is a velocity scale corresponding to the rate at which collision and coalescence destroy surface area. A detailed derivation of these terms can be found in Vallet's original description of the model.⁷ Since the model was initially published, several alternative forms of this equation have been proposed to better resolve differences in primary and secondary atomization.¹¹ Knowledge of Σ allows the prediction of the Sauter mean diameter and the droplet number density via

$$d_{32} = \frac{6\bar{\rho}\tilde{Y}}{\rho_l \bar{\Sigma}} \quad (9)$$

and

$$n = \frac{\rho_l^2 \bar{\Sigma}^3}{36\pi \bar{\rho}^2 \tilde{Y}^2} \quad (10)$$

A transport equation having this form predicts an equilibrium value of Σ when $\bar{\Sigma}_{eq} = \frac{\tau_{destr}}{\tau_{prod}}$

Diffusion liquid flux closure

The ability of the model to effectively predict the structure of the liquid film is governed by the closure of the diffusion flux in the volume fraction transport equation. Vallet et al. derived an algebraic relation for this flux by first considering the following transport equation for the mass fluctuation Y' derived via the Reynolds averaging process.¹⁰

$$\frac{\partial \bar{\rho} \widetilde{u'_i Y'}}{\partial t} + \frac{\partial \bar{\rho} u_j \widetilde{u'_i Y'}}{\partial x_j} = - \frac{\partial}{\partial x_j} \left(\bar{\rho} \widetilde{u'_j u'_i Y'} + p' \bar{Y}' \delta_{ij} \right) - \bar{\rho} \widetilde{u'_j u'_i} \frac{\partial \tilde{Y}}{\partial x_j} - (1 - \gamma^Y) \bar{\rho} \widetilde{u'_j Y'} - \left(1 - \gamma'^Y \right) \frac{\partial p}{\partial x_i} - \rho \frac{a_1}{\tau_t} \widetilde{u'_i Y'} \quad (11)$$

The first term on the right hand side corresponds to the diffusion of mass fluctuations, the following three terms to production, and the final term to destruction.

Equation 11 assumes that $p' \frac{\partial \bar{Y}'}{\partial x_i}$ can be expressed as

$$p' \frac{\partial \bar{Y}'}{\partial x_i} = -\bar{\rho} \frac{a_1}{\tau_t} \widetilde{u'_i Y'} + \gamma^Y \bar{\rho} \widetilde{u'_j Y'} + \gamma'^Y \bar{Y}' \frac{\partial p}{\partial x_i} \quad (12)$$

where τ_t is the integral turbulence timescale and a_1 , γ^Y and γ'^Y are constants. Assuming dominance by the production and destruction terms yields the following algebraic closure.

$$\bar{\rho} \widetilde{u'_i Y'} = -\frac{\tau_t}{a_1} \left[\bar{\rho} \widetilde{u'_j u'_i} \frac{\partial \tilde{Y}}{\partial x_j} + (1 - \gamma^Y) \bar{\rho} \widetilde{u'_j Y'} \frac{\partial u_i}{\partial x_j} + \left(1 - \gamma'^Y \right) \bar{Y}' \frac{\partial p}{\partial x_i} \right] \quad (13)$$

where \bar{Y}' is defined exactly as

$$\bar{Y}' = \bar{\rho} \tilde{Y} \left(1 - \tilde{Y} \right) \left(\frac{1}{\rho_l} - \frac{1}{\rho_g} \right) \quad (14)$$

Under the further assumption that diffusion is dominated by the first term on the right hand side of Equation 13, this results in the classical Fick's law of diffusion

$$\bar{\rho} \widetilde{u'_i Y'} = \frac{\mu_t}{Sc} \frac{\partial \tilde{Y}}{\partial x_i} \quad (15)$$

Demoulin proposed the following term to capture the enhancement of Rayleigh-Taylor instability growth caused by the presence of a large density gradient.

$$\bar{\rho} \widetilde{u'_i Y'} = \rho \left[\frac{\nu_t}{Sc} + C_p \frac{k^2}{\epsilon} \bar{\rho} \left(\frac{1}{\rho_g} - \frac{1}{\rho_l} \right) \tilde{Y} (1 - \tilde{Y}) \right] \frac{\partial \tilde{Y}}{\partial x_i} \quad (16)$$

The inclusion of this term has proven successful in resolving the primary liquid core size for both diesel¹¹ and coaxial⁸ injections.

Implementation

The $\Sigma - Y$ model was implemented using the OpenFOAM software framework.¹² The implementation uses a fully parallelized finite-volume method generalized to arbitrary convex polyhedral cells in two and three dimensions. Discretization methods are selected at run-time and include over thirty choices of flux limiting.

A segregated pressured-based PISO method¹³ has been implemented to update variables at each timestep by:

- Solving the continuity equation using the volumetric flux from the previous timestep
- Solving the species transport equation using the mass flux predicted by the continuity equation
- Solving the momentum equation to predict the current volumetric flux
- Iteratively solving the pressure equation until the velocity field satisfies the continuity equation
- Updating continuity and species transport equations
- Either iterate to correct for coupling between species transport and pressure equation, or procede to next timestep

To derive the pressure equation, the single phase incompressible pressure equation typically implemented in OpenFOAM¹⁴ was altered to account for variable density effects. The semi-discretized form of the momentum equation is defined as

$$a_p \mathbf{U}_p = \mathbf{H}(\mathbf{U}) - \nabla p \quad (17)$$

where $\mathbf{H}(\mathbf{u})$ consists of two parts: the advection terms which includes the matrix coefficients of neighboring cells multiplied by the corresponding velocities and the source term, accounting for all point sources in the momentum equations (such as gravity, body forces, etc.).

$$\mathbf{H}(\mathbf{U}) = \sum_N a_N \mathbf{U}_N + \frac{\mathbf{U}^0}{\Delta t} \quad (18)$$

Equation 17 is rearranged and interpolated to faces. Taking the divergence of this gives

$$\nabla \cdot (\mathbf{U}_p)_f = \nabla \cdot \left(\frac{1}{a_p} \mathbf{H}(\mathbf{U})_f \right) - \nabla \cdot \left(\frac{1}{a_p} \nabla p \right)_f \quad (19)$$

The effect of variable density is then coupled to the pressure equation via Equation 6, the continuity equation and the chain rule

$$\nabla \cdot (\mathbf{U}_p)_f = -\frac{1}{\rho} \frac{\partial \rho}{\partial \tilde{Y}} \frac{D\tilde{Y}}{Dt} = \left(\frac{1}{\rho_l} - \frac{1}{\rho_g} \right) \widetilde{\rho u'_i \tilde{Y}'} \quad (20)$$

Solving the equation

$$\nabla \cdot \left(\frac{1}{a_p} \mathbf{H}(\mathbf{U})_f \right) - \nabla \cdot \left(\frac{1}{a_p} \nabla p \right)_f = \left(\frac{1}{\rho_l} - \frac{1}{\rho_g} \right) \widetilde{\rho u'_i \tilde{Y}'} \quad (21)$$

and updating the fluxes will give a velocity field that satisfies the continuity equation.

Results

The conditions and geometry for this particular study are discussed in Lightfoot et al.¹ Specifically, the ONPNTN geometry was considered under the operating conditions denoted in Table 1. The computational boundary conditions were set by matching liquid flow rate and gas flow rate, assuming a uniform incoming velocity profile, and a fixed total pressure condition at the injector outlet. It is important to note that for several of the higher momentum ratio cases, the gas flowrates yield flow velocities in the transonic regime,

rendering the assumption of incompressibility questionable. Experimental measurements of the total pressure at the inlet suggest that choking is not occurring, but the difference in gas density could substantially alter the momentum ratio at the interface. To obtain an estimate of the effect of compressibility, a separate single-phase, turbulent, compressible flow solver was used to compare the predicted velocity and density fields. This solver obtained a range of densities from $0.98 - 1.4 \frac{kg}{m^3}$, suggesting a 15% possible difference in gas momentum at the interface.

Table 1. Simulation conditions

Case name	ρ_{gas} $\frac{kg}{m^3}$	ρ_{liq} $\frac{kg}{m^3}$	$U_{gas,in}$ $\frac{m}{s}$	$U_{liq,in,z}$ $\frac{m}{s}$	$U_{liq,in,\theta}$ $\frac{m}{s}$	p_{out} kPa
ONPNTN-a1	1.2	999	300	0.35	4.2	101.325
ONPNTN-b1	1.2	999	153	0.52	6	101.325

In the computation, the domain is in two-dimensional polar coordinates (r, z) , with $r > 0$, with a two-dimensional mesh containing eleven thousand cells. The assumption of axisymmetric flow was validated by performing a 3D simulation of a 90° sector of the full geometry. While the experimental photographs did exhibit asymmetry between the top and bottom film profiles, this has been attributed to experimental conditions and is discussed by Schumaker et al.¹⁵

Turbulence was modeled using both a classical two equation $k - \epsilon$ model and the realizable $k - \epsilon$ model developed by Shih.¹⁶ All previous implementations^{7, 11, 17, 18} of the $\Sigma - Y$ model have used the $k - \epsilon$ model because of its stability and ability to resolve mixing layers, which was well suited for the plain orifice and coaxial arrangements previously considered. The $k - \epsilon$ model is well known to be unable to accurately predict the recirculation zone following a backward facing step. While any turbulence model based on the Boussinesque assumption will have difficulty capturing the effect of swirl, the realizable $k - \epsilon$ model should be capable of more accurately resolving the strength of the recirculation zone, which is assumed to be the dominant turbulent mechanism affecting the film profile.

Simulations were run using the standard $k - \epsilon$ model for the ONPNTN-b1 case using the default value for the Schmidt number of 0.9. Figure 4 shows the resulting pressure and volume fraction profiles. Figure 5 shows an instantaneous photograph of the injector under the same operating conditions. The experimental photograph suggests that the liquid should be pushed up against the backward facing step by the recirculation zone, and the lack of this feature suggests that the model is underpredicting the turbulent dispersion. Also visible in Figure 4 is a static pressure gradient caused by the centripetal acceleration present in the swirling liquid film.

Preliminary results using Demoulin et al's modified closure (Equation 16) further underestimated the film length. This is attributed to the fact that, for the swirling liquid film under consideration, the centripetal acceleration acting upon the interface has a stabilizing effect that suppresses the growth of the Rayleigh-Taylor type instability.

As a first-order approximation of the reduced turbulent dispersion caused by the swirl, the Schmidt number was increased to determine its effect upon the liquid film profile. Figure 6 demonstrates that increasing the Schmidt number from the standard value of 0.9 up to a value of 20 allows the model to accurately reproduce the experimental data.

Figure 7 gives a similar parametric study of the Schmidt number when the realizable $k - \epsilon$ turbulence closure is used instead. For this case, a Schmidt number of only 15 provides a more accurate representation of the film profile. This suggests that the standard $k - \epsilon$ model is overpredicting the liquid dispersion, as expected.

To characterize the generality of these results, a case with a significantly shorter film length was investigated. Figure 8 shows an experimental photograph of the film profile. For this case, the light scattering at the interface is substantially more diffuse, suggesting the presence of more turbulent mixing. Figures 9 and 10 compare the predicted liquid profiles to the time-averaged experimental data. Both simulations show good initial agreement, but are abruptly cut short as a recirculation zone forms at the end of the liquid film (Figure 11). As expected, the realizable $k - \epsilon$ model comes closer to predicting the experimental result but also fails to accurately resolve the correct behavior near the recirculation zone. In Beheshti et al.'s assessment of the $\Sigma - Y$ model,¹⁸ they noted that in its current form the model is incapable of accurately

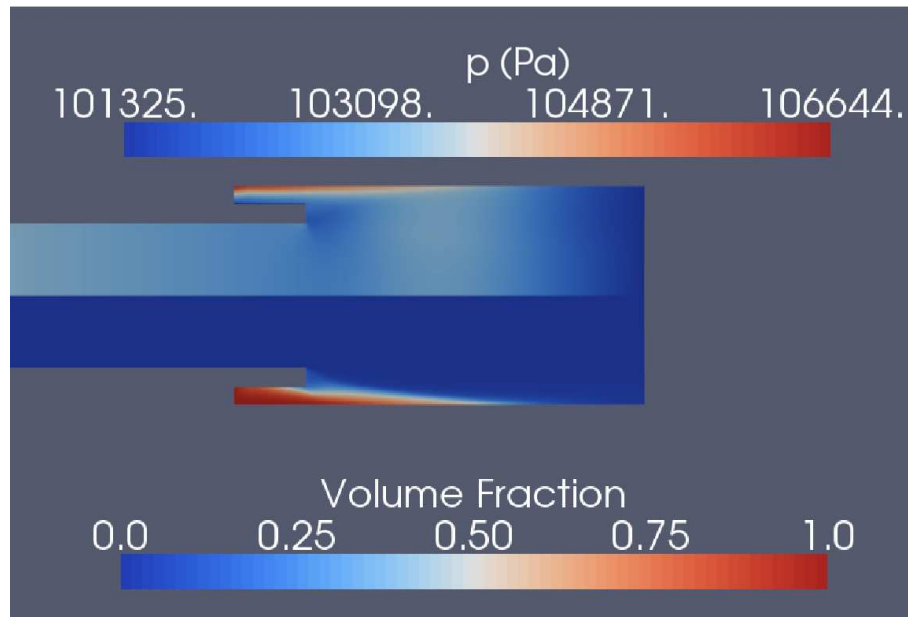


Figure 4. Static pressure and volume fraction profile for ONPNTN-b1 case

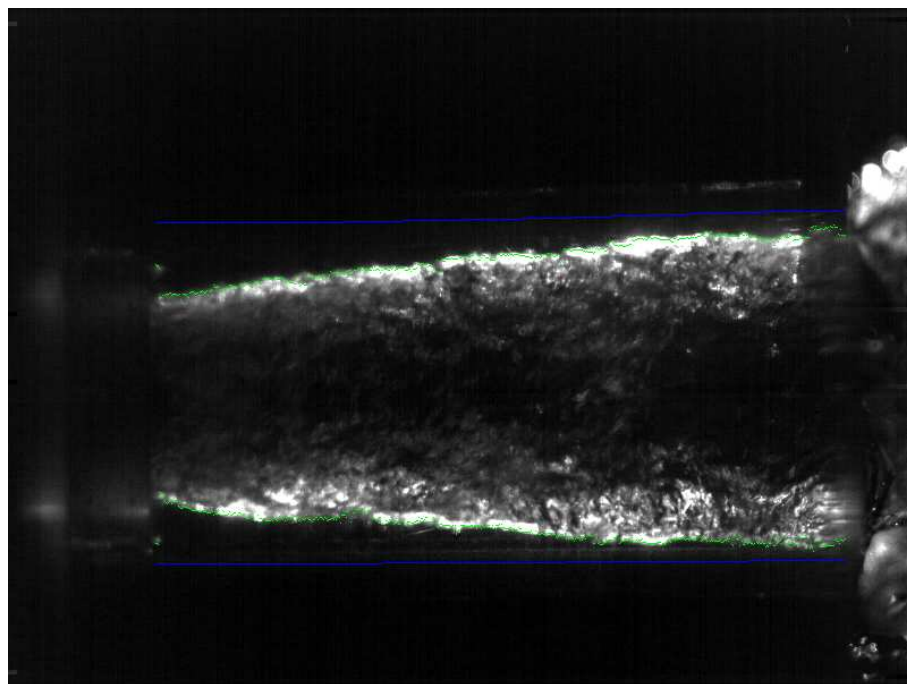


Figure 5. Experimental photograph of liquid profile for ONPNTN-b1 case

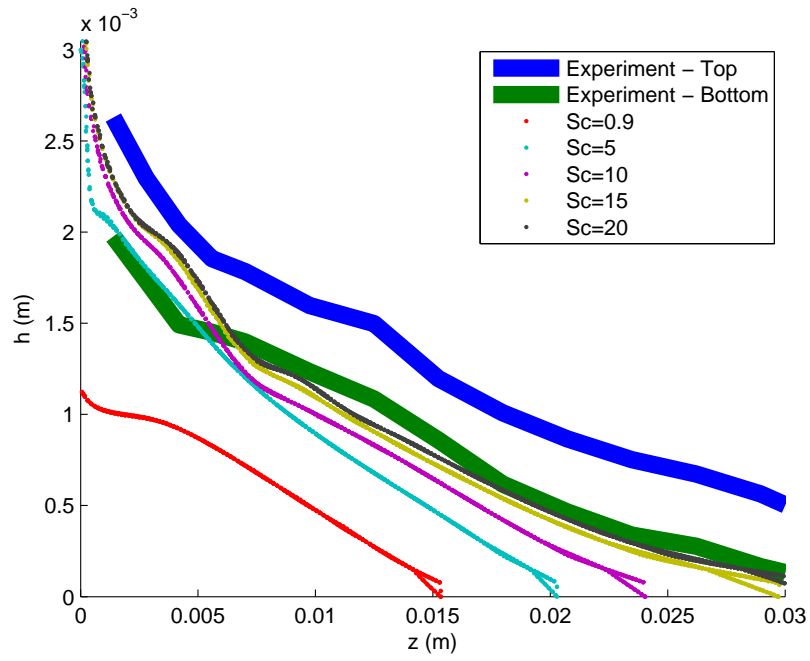


Figure 6. Iso-contours of $\bar{Y} = 0.5$ compared to experimental profiles for standard $k - \epsilon$ closure

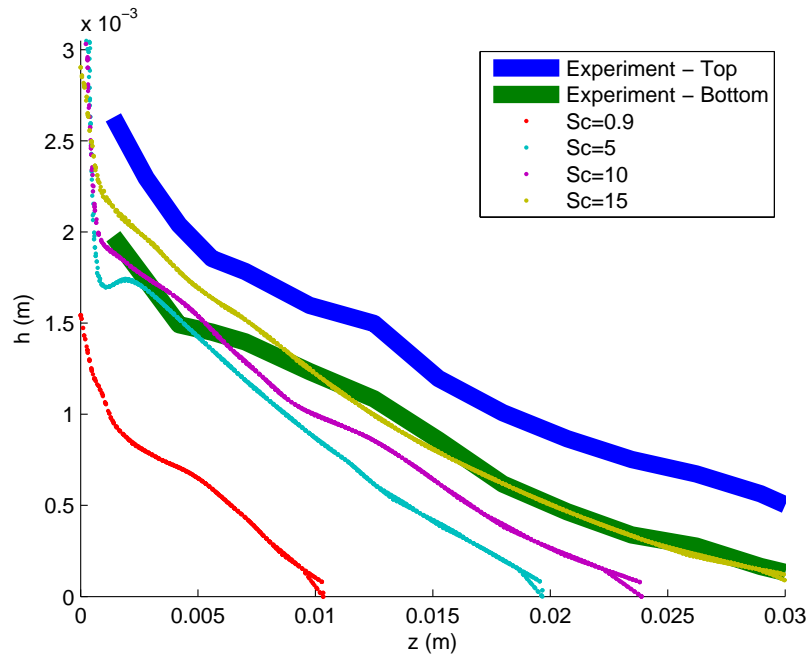


Figure 7. Iso-contours of $\bar{Y} = 0.5$ compared to experimental profiles for realizable $k - \epsilon$ closure

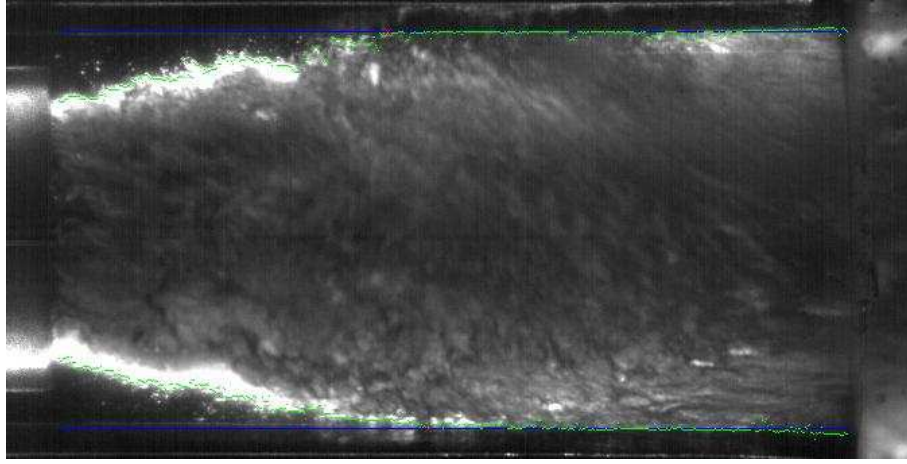


Figure 8. Experimental photograph of liquid profile for ONPNTN-a1 case

resolving flows with areas of large recirculation. In this scenario, the fundamental assumption that the flow is acting at large Reynold's and Weber number is violated, as the velocity within the recirculation zone is substantially less than the free-stream velocity.

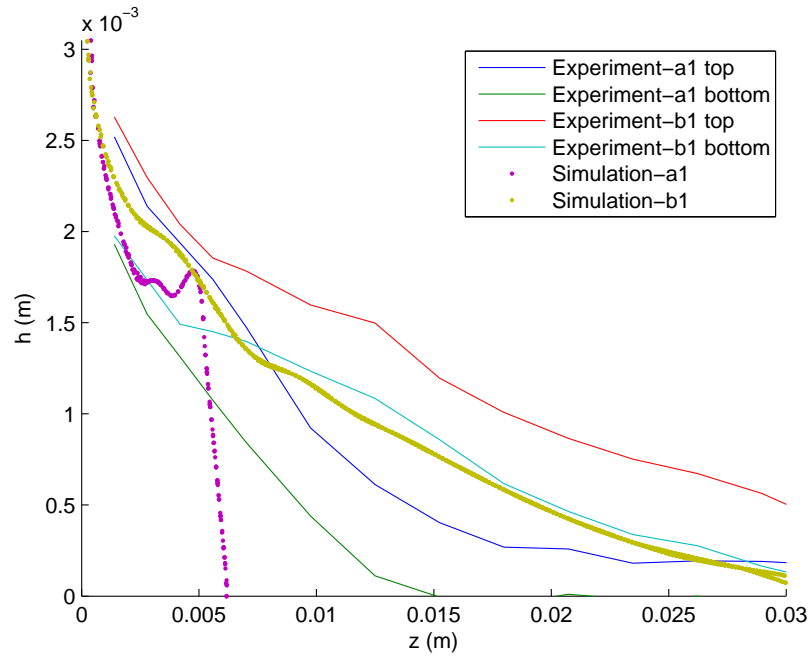


Figure 9. Iso-contours of $\bar{Y} = 0.5$ compared to experimental profiles for standard $k - \epsilon$ closure

Conclusions

Resolving the complex fluid mechanics occurring within the cup of a GCSC presents numerous experimental and modeling challenges. The correspondence of both the experimental and computational results is consistent with the film extent being determined by turbulent transport. For CFD simulation, rather than trying to resolve the wide variety of scales present in the cup, the resolved scales can be treated with conservation laws and the unresolvable turbulence/interface interaction can be represented by models. While the model was able to predict low momentum ratio film profiles, it failed to predict film structure when the gas flowrate was increased and recirculation zones became more pronounced. This shortcoming has not yet

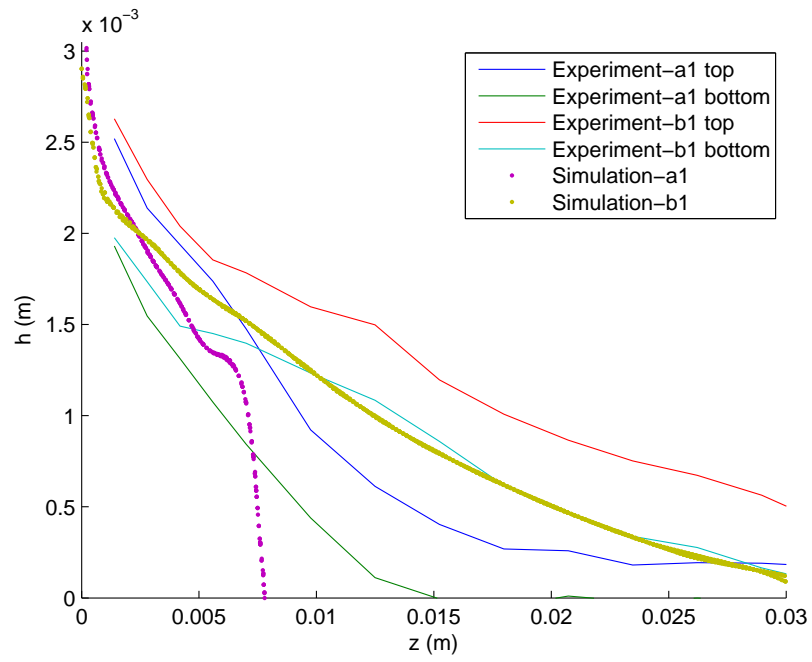


Figure 10. Iso-contours of $\bar{Y} = 0.5$ compared to experimental profiles for realizable $k - \epsilon$ closure

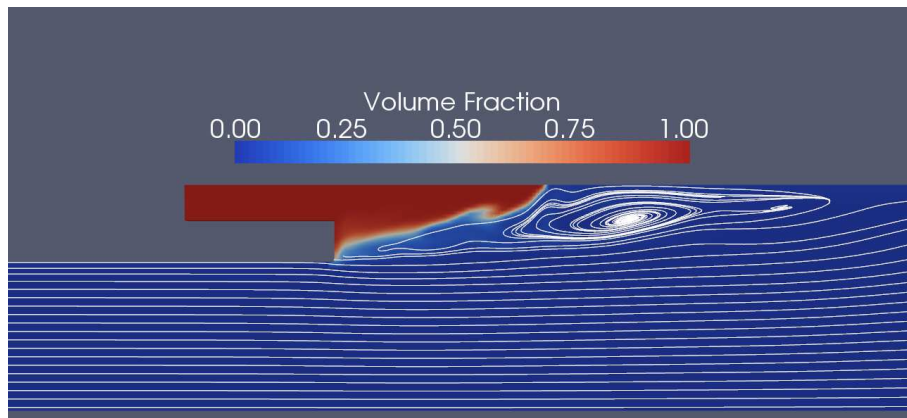


Figure 11. Instantaneous film profile and streamlines show the presence of a recirculation zone for the ONPNTN-a1 case

been observed in other injector arrangements. For this model to be used as a reliable predictor of film length, higher order modeling closures for the turbulent flux must be used to resolve the complex recirculation zone interactions.

References

- ¹Lightfoot, M., Danczyk, S., and Talley, D., “Scaling of Gas-Centered Swirl-Coaxial Injectors,” Tech. rep., Air Force Research Laboratory, 2009.
- ²Ibrahim, A. and Jog, M., “Effect of Liquid and Air Swirl Strength and Relative Rotational Direction on the Instability of an Annular Liquid Sheet,” *Acta Mechanica*, Vol. 186, 2006, pp. 113–133.
- ³Pope, S., *Turbulent Flows*, Cambridge University Press, New York, NY, USA, 2000.
- ⁴Rahman, S., Pal, S., and Santoro, R., “Swirl Coaxial Atomization: Cold-flow and Hot-fire Experiments,” *American Institute of Aeronautics and Astronautics*, 1995.
- ⁵Cohn, R., Strakey, P., Bates, R., Tallet, D., Muss, J., and Johnson, C., “Swirl Coaxial Injector Development,” *AIAA Aerospace Sciences Conference*, 1995.
- ⁶Soltani, M., Ghorbanian, K., Ashjaee, M., and Morad, M., “Spray characteristics of a liquidliquid coaxial swirl atomizer at different mass ow rates,” *Aerospace Science and Technology*, 2005.
- ⁷A. Vallet, A. A. B. and Borghi, R., “Development of a Eulerian Model for the “Atomization” of a Liquid Jet,” *Atomization and Sprays*, Vol. 11, 2001, pp. 619–642.
- ⁸Demoulin, F., Beau, P., Blokkeel, G., Mura, A., and Borghi, R., “A New Model for Turbulent Flows with Large Density Fluctuations: Application to Liquid Atomization,” *Atomization and Sprays*, Vol. 17, 2007, pp. 315–345.
- ⁹Morel, C., “On the surface equations in two-phase ows and reacting single-phase ows,” *International Journal of Multiphase Flow*, 2007.
- ¹⁰Vallet, A. and Borghi, R., “Modélisation Eulerienne de L’atomisation d’un Jet Liquide,” *C. R. Acad. Sci*, Vol. 327, 1999, pp. 1015–1020.
- ¹¹Lebas, R., Menard, T., Beau, P., Berlemont, A., and Demoulin, F., “Numerical simulation of primary break-up and atomization: DNS and modeling study,” *International Journal of Multiphase Flow*, Vol. 35, 2009, pp. 247–260.
- ¹²Weller, H. G., Tabor, G., Jasak, H., and Fureby, C., “A Tensorial Approach to Computational Continuum Mechanics Using Object–Oriented Techniques,” *Computers in Physics*, Vol. 12, No. 6, 1998, pp. 620–63.
- ¹³Ferziger, J. and Peric, M., *Computational Methods for Fluid Dynamics*, Springer, Berlin, 2002.
- ¹⁴Jasak, H., *Error Analysis and Estimation for the Finite Volume Method with Applications to Fluid Flows*, Ph.D. thesis, Imperial College, 1996.
- ¹⁵S. Alexander Schumaker, S. A. D. and Lightfoot, M. D., “Effect of Parameter Variation on Nonuniformities in Gas-Centered Swirl-Coaxial Injectors,” *AIAA Conference Proceedings*, 2010.
- ¹⁶Shih, T.-H., Liou, W. W., Shabbir, A., Tang, Z., and Zhu, J., “A New k-epsilon Eddy Viscosity Model for High Reynolds Number Turbulent Flows,” *Computers and Fluids*, 1995.
- ¹⁷Jay, S., Lacas, F., and Candel, S., “Combined surface density concepts for dense spray combustion,” *Combustion and Flame*, Vol. 144, 2006, pp. 558–577.
- ¹⁸Beheshti, N., Burluka, A., and Fairweather, M., “Assessment of $\Sigma - Y_{liq}$ model predictions for air-assisted atomisation,” *Theoretical and Computational Fluid Dynamics*, Vol. 21, 2007, pp. 381–397.

Acknowledgments

The authors acknowledge funding under Air Force contract FA9550-08-C-0030.